SciPost Physics

Submission

Pair binding and Hund's rule breaking in high-symmetry fullerenes

Roman Rausch, Christoph Karrasch

Technische Universität Braunschweig, Institut für Mathematische Physik,
Mendelssohnstraße 3, 38106 Braunschweig, Germany

November 14, 2025

Abstract

Highly-symmetric molecules often exhibit degenerate tight-binding states at the Fermi edge. This typically results in a magnetic ground state if small interactions are introduced in accordance with Hund's rule. In some cases, Hund's rule may be broken, which signals pair binding and goes hand-in-hand with an attractive pair-binding energy.

We investigate pair binding and Hund's rule breaking for the Hubbard model on high-symmetry fullerenes C_{20}, C_{20}, C_{40}, and C_{60} by using large-scale density-matrix renormalization group calculations. We exploit the SU(2) spin symmetry, the U(1) charge symmetry, and optionally the $\mathbb{Z}_N$ spatial rotation symmetry of the problem.

For C_{20}, our results agree well with available exact-diagonalization data, but our approach is numerically much cheaper. We find a Mott transition at $U_c \sim 2.2t$, which is much smaller than the previously reported value of $U_c \sim 4.1t$ that was extrapolated from a few datapoints. We compute the pair-binding energy for arbitrary values of U and observe that it remains overall repulsive.

For larger fullerenes, we are not able to evaluate the pair binding energy with sufficient precision, but we can still investigate Hund's rule breaking. For C_{28}, we find that Hund's rule is fulfilled with a magnetic spin-2 ground state that transitions to a spin-1 state at $U_{c,1} \sim 5.4t$ before the eventual Mott transition to a spin singlet takes place at $U_{c,2} \sim 11.6t$. For C_{40}, Hund's rule is broken in the singlet ground state at half filling, but is restored if the system is doped with one electron. Hund's rule is also broken for C_{60}, and the doping with two or three electrons results in a minimum-spin state.

Our results ~~support~~ are consistent with an electronic mechanism of superconductivity for C_{60} lattices. We speculate that the high geometric frustration of small fullerenes is detrimental to pair binding.

1 Introduction

Hund's rule is a well-known effect from atomic physics: An electronic shell that is degenerate in the one-particle picture will in fact split up upon introducing interactions, and the lowest-energy state features a maximum spin [1], which reduces interelectronic repulsion [2]. Intuitively, same-spin electrons avoid getting close to each other by virtue of the Pauli principle, while opposite-spin electrons can occupy the same space. In nuclei, the interfermionic interactions are attractive as a result of the strong force and the opposite situation occurs: An even number of nucleons in a degenerate shell will always form a singlet state [3, 4].

Hund's rule is mostly valid in molecules as well: If a free-electron model on some molecular geometry produces degenerate shells, the inclusion of weak interactions will typically lead to a maximum-spin ground state. For some molecules, however, Hund's rule may be broken, which signals effective attraction similar to nuclei [5]. This is a case of interest because molecules with attractive pair binding may serve as building blocks for molecular lattices with global superconductivity, with a purely electronic mechanism that can be understood from the individual molecules alone.

Pair binding can be quantified by evaluating the pair binding energy

$$E_b = E_0(N_{\text{tot}}) + E_0(N_{\text{tot}} + 2) - 2E_0(N_{\text{tot}} + 1), \tag{1}$$

where $E_0(N_{\text{tot}})$ is the state with the lowest overall energy of an isolated molecule in the sector with N_{tot} electrons. If $E_b < 0$, then an ensemble of uncoupled molecules will prefer a state with doped electrons paired up on the same molecule, rather than being split on separate ones. Weak intermolecular hopping is then expected to render a molecular lattice superconducting.

It is known that a large shell degeneracy, which is generally related to a non-Abelian molecular symmetry, is a key ingredient for pair binding [5]. High-symmetry molecules can also more easily crystallize into lattices. The most interesting molecules are thus the highly symmetric ones, e.g., those forming Platonic or Archimedean solids. Of particular importance is the C_{60} fullerene, which is an Archimedean solid (truncated icosahedron, symmetry group I_h). It is insulating at half filling (i.e., it features a full shell, and thus a singlet ground state) and has a threefold degenerate lowest unoccupied molecular orbital (LUMO), which can be chemically doped (see Tab. 1). Experimentally, a face-centered cubic (fcc) lattice of electron-doped C_{60} molecules shows superconductivity with a critical temperature of $T_c \approx 30 - 40K$ [6, 7]. This is relatively high for a phononic mechanism, so that an electronic mechanism is also being debated [8].

Since there is one active p orbital per carbon atom, the minimal model that incorporates correlations and allows for the breaking of spin degeneracy is the single-band Hubbard model. It has been widely studied for fullerenes [8–16] and was shown to reproduce the

single-particle spectra reasonably well [17]. A more realistic model would involve long-ranged Coulomb interactions as well as additional effects like Jahn-Teller distortion or a coupling to phonons. However, before one ascends the hierarchy of ever more sophisticated approaches, one should gain clarity with respect to the predictions of the basic Hubbard model.

The Hubbard Hamiltonian is given by

$$H = -\sum_{ij\sigma} t_{ij} c_{i\sigma}^{\dagger} c_{j\sigma} + \text{h.c.} + U \sum_{i} n_{i\uparrow} n_{i\downarrow}. \tag{2}$$

Here, t_{ij} is the hopping matrix, $c_{i\sigma}^{\dagger}$ ($c_{i\sigma}$) is the creation (annihilation) operator for an electron with spin $\sigma = \uparrow, \downarrow$ at atom i of the molecule, U is the onsite Coulomb interaction, and $n_{i\sigma} = c_{i\sigma}^{\dagger} c_{i\sigma}$ is the electron density. One typically employs the tight-binding approximation where t_{ij} takes the value t between nearest neighbors. We set it to be the unit of energy $t = 1$ from now on.

An interesting high-symmetry Hubbard cluster is the truncated tetrahedron ($L = 12$ sites), since it can be regarded as a coarse-grained simplified version of C_{60} (see Fig. 1). Using exact diagonalization (ED), White et al. demonstrated attractive pair binding with a peak of $E_b \sim -0.02$ for C_{12} around $U \sim 2$ within the Hubbard model [5]. Similar attractive behaviour was found for the cube ($L = 8$). The smallest proper fullerene is C_{20}, which is solvable by exact diagonalization, but the effort is substantial. Surprisingly, no attractive pair binding was observed [16, 18]. For C_{60}, which is very difficult to tackle theoretically, conflicting results were obtained: Extrapolations from perturbation theory predicted a minimum-spin doped state [9,10], while QMC calculations yielded a maximum-spin state [14]. Density-matrix renormalization group (DMRG) calculations for the related simpler $t - J$ model predict a minimum-spin state [19]. Finally, there is a gap in the literature when it comes to the intermediate fullerenes C_n with $20 < n \leq 60$ (or, indeed, larger ones with $n > 60$).

This situation motivates us to address the following questions: i) Is Hund's rule fulfilled for the intermediate fullerenes between C_{20} and C_{60}? Because of the high-symmetry requirement, this reduces the candidates to just C_{20} and C_{40} (both of T_d symmetry, see Fig. 1). ii) What can we learn about the full Hubbard model on C_{60}? For this problem, we give our best possible estimate using large-scale DMRG computations. iii) What is the reason that some molecules exhibit Hund's rule breaking, while others do not?

This paper is organized as follows: In Sec. 2 we outline the technical details of our DMRG calculations. Then we discuss results for C_{20}, C_{28}, C_{40}, and C_{60} in Sec. 3, 4, 5, 6, respectively, before concluding in Sec. 7. The sections on C_{20} and C_{60} also contain discussions of previously published results. In App. A, we present the strong-coupling (Heisenberg) limit for reasons of completeness. The explanation of how to exploit the $\mathbb{Z}_N$ rotational symmetry is presented in App. B. Finally, App. C documents our raw data (ground-state energies as a function of the spin and particle number) as a reference and for potential benchmarks with other methods.

2 Technical details

We investigate finite molecular geometries within the pure Hubbard model (2) by using the DMRG method, which approximates the wavefunction variationally within the class of matrix-product states (MPS) [20]. The DMRG exploits the property that physical ground states are only entangled locally (area law) and can thus be accurately represented by MPS. The key control parameter is the so-called bond dimension χ, which is related to the number
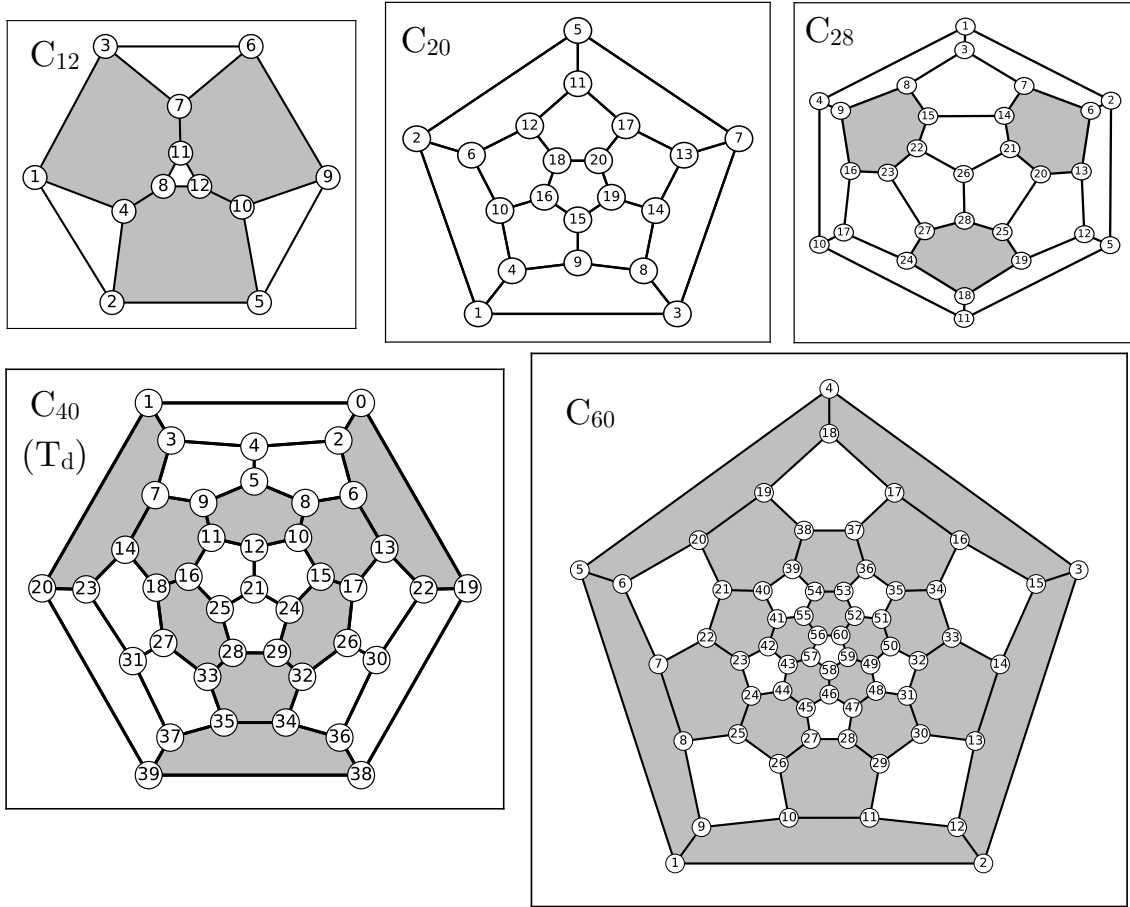
Figure 1: Schlegel diagrams (nearest-neighbor graphs) of the high-symmetry fullerenes studied in this work. The hexagon faces are shaded grey for clarity, illustrating the full separation of the frustrated pentagon faces for C_{12} and C_{60}.
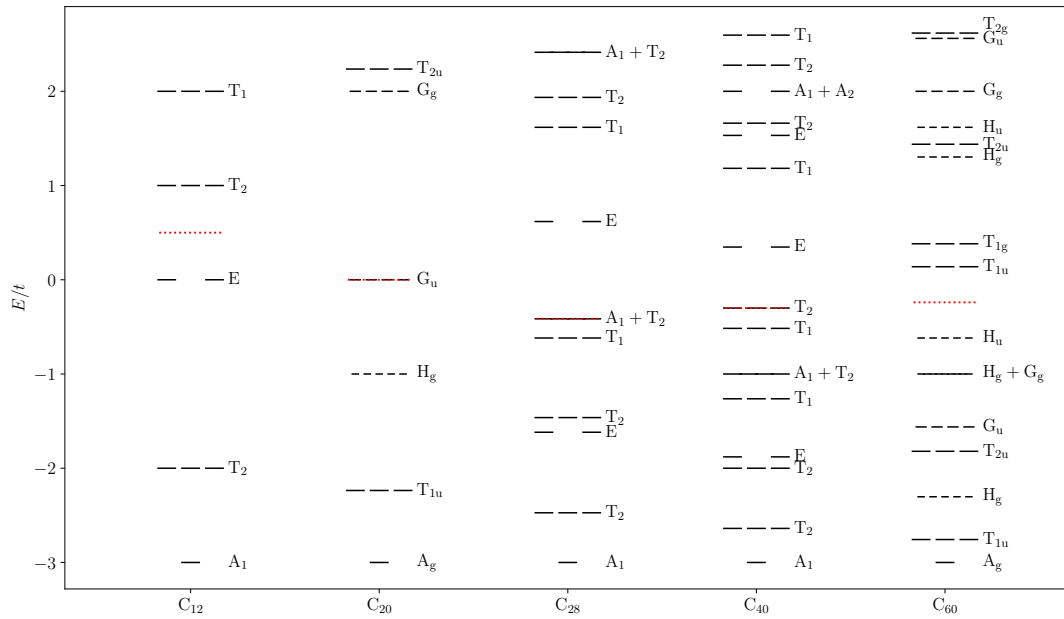
Figure 2: Energy levels of the tight-binding (Hückel) model for the high-symmetry fullerenes studied in this work (see Fig. 1) along with their irreducible representations. The red dotted line marks the Fermi energy at half filling.

molecule	sym.	W	shell filling	irrep	degeneracy	orbital	r
cube	O_h	6.0	closed, $\Delta = 2.0$	T_{2g}	3	LUMO	4
C_{12}	T_d	5.0	closed, $\Delta = 1.0$	T_2	3	LUMO	5
C_{20}	I_h	5.236	2	G_u	4	HOMO	6
C_{28}	T_d	5.414	4	$T_2 + A_1$	4	HOMO	7
C_{40}	T_d	5.596	2	T_2	3	HOMO	9
C_{60}	I_h	5.618	closed, $\Delta = 0.757$	T_{1u}	3	LUMO	10

Table 1: Symmetry and bandstructure properties ($U = 0$; tight-binding or Hückel limit) of high-symmetry molecules, obtained by diagonalizing the hopping matrix t_{ij}. W denotes the bandwidth, i.e., the difference between highest and lowest eigenenergy. The shell filling is the number of electrons in the highest occupied molecular orbital (HOMO) for open shells, and Δ is the HOMO-LUMO gap closed shells. The degeneracy and irrep label refer to the LUMO (HOMO) for closed (open) shells. The hopping range r is the graph bandwidth of t_{ij} after applying the reverse Cuthill McKee algorithm, which influences the complexity of the problem for the real-space DMRG.

of variational parameters. The area law renders the application to one-dimensional systems particularly efficient, but all finite systems necessarily only have finite entanglement which can be captured by a sufficiently large χ. Hence, the method can also yield very accurate results for molecules that are not too large [19,21–24]. For this reason, it is widely employed in quantum chemistry [25].

To gauge the accuracy of our DMRG calculations, we use the energy variance per site:

$$\text{var}(E)/L = \left| \langle H^2 \rangle - \langle H \rangle^2 \right|/L, \tag{3}$$

which should vanish for an exact eigenstate and thus serves as a measure of how far one is from the exact solution. In cases where the exact energy is known, one typically finds that the variance is linearly related to the true error [26], and we will therefore use this as an extrapolation scheme for the energy. Error bars are defined as the standard error of the extrapolated energy (more precisely, as the square root of the corresponding element of the covariance matrix resulting from the least-squares fit). We employ the two-site DMRG algorithm to grow the bond dimension on the first iterations before switching to the cheaper one-site algorithm with fluctuations [27]. The DMRG requires a mapping of the sites to a one-dimensional chain, and the molecular geometry generates long-range hopping terms whose range we minimize by applying the reverse Cuthill-McKee algorithm to the graph t_{ij} [28]. The maximum hopping range for our systems is shown in Tab. 1. The higher the value, the more complex the problem becomes for the DMRG. The most difficult case considered here is C_{60} with a range of 10, which is roughly equivalent in complexity to a 10-leg ladder. Finally, one must find a compact matrix-product operator representation [29].

The binding energy in Eq. (1) is small compared to the hopping t, typically $O(10^{-2}t)$, but is itself a result of the difference of large numbers.[1] Thus, it is crucial that the computed energies should be as accurate as possible, preferably to at least 4 digits. In order to boost the performance of the DMRG, we exploit the U(1) charge symmetry as well as the SU(2) spin symmetry [30]. This approach also allows us to directly compute the ground state energy $E_0(N_{\text{tot}}, S_{\text{tot}})$ in the different charge and spin sectors labelled by N_{tot} and S_{tot}, respectively. Half filling corresponds to $N_{\text{tot}} = L$. We optionally exploit the $\mathbb{Z}_N$ rotational symmetry (more commonly denoted C_n in the realm of chemistry), which is analogous to

---

[1] We note that $t \sim 2.8\,\text{eV}$ for carbon, which places a pair-binding energy of $E_b \sim 10^{-2}t$ on the scale of room temperature ($0.025\,\text{eV}$), which is quite large in terms of absolute numbers.
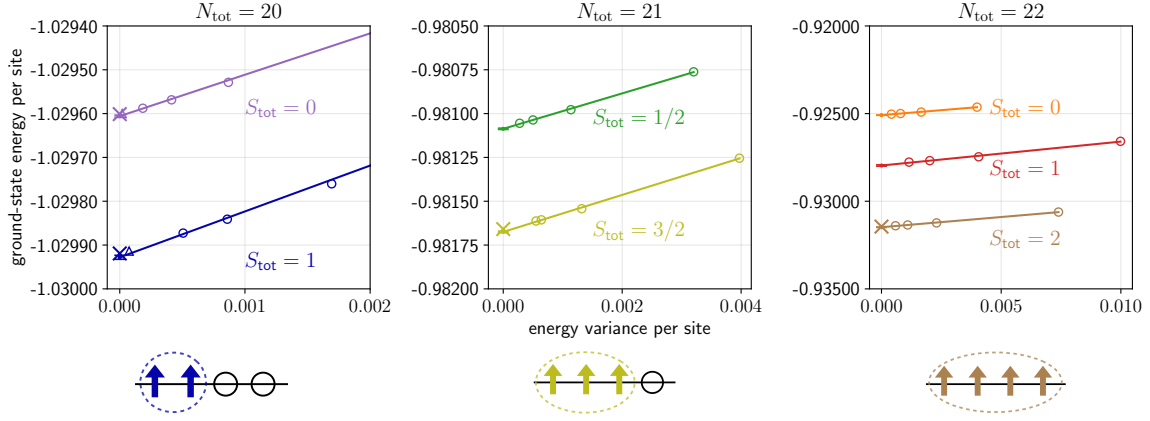
Figure 3: DMRG data for the ground-state energy per site for C_{20} at $U = 2$ in various sectors of the particle number N_{tot} and the total spin S_{tot}. Small circles: SU(2)×U(1)-symmetric calculation, bond dimensions $\chi_{SU(2)} \leq 10\,000$. Triangles: SU(2)×U(1)×$\mathbb{Z}_5$-symmetric calculation, $\chi_{SU(2)} = 15\,000$ (one datapoint in selected sectors). The DMRG values are linearly extrapolated in the variance per site (which decreases with increasing bond dimension), and ; the large circles indicate the extrapolated results as well the error bars associated with the fit (which are also shown but are barely visible in this case)here. The crosses show the reference values from exact diagonalization. The pictures below the plots schematically visualize the filling of the HOMO (arrows: electrons, black circles: empty levels). Hund's rule holds true at any filling.

the case of the transverse momentum for cylinders [31–33] and is explained in App. B in detail.

We note that the exploitation of the SU(2) spin symmetry has the effect that the bond dimension $\chi_{SU(2)}$ used in the numerics corresponds to a larger effective bond dimension if only spin-U(1) is exploited, i.e., $\chi = g\chi_{SU(2)}$, with a gain factor of $g = 3 \pm 0.2$ in our case. It also allows us to directly target the total spin quantum number S_{tot} instead of merely its projection S_{tot}^z.

The advantage of exploiting the $\mathbb{Z}_N$ symmetry is that the quantum number blocks in the MPS representation shrink roughly by a factor of N, so that one can work with larger bond dimensions. A downside is the need to perform the calculations for all possible values of J (which is at least parallelizable). Another disadvantage is the need to switch from real to complex numerics. The fundamental question, however, is whether the entanglement increase due to the additional nonlocal terms will be fully compensated by the increased bond dimension. For this reason, the benefit of using $\mathbb{Z}_N$ symmetry is *a priori* not clear and depends on the geometry of the system. For the fullerenes, we find that exploiting $\mathbb{Z}_N$ is advantageous for C_{20}, C_{28}, and C_{40} but not for the most interesting case of C_{60}.

3 Molecule C_{20}

The properties of the (extended) Hubbard model on C_{20} were investigated in detail using large-scale ED both for the undistorted geometry (I_h symmetry) and including Jahn-Teller distortion (reduction to D_{3d} symmetry) [16]. Despite the exploitation of both the spin-U(1) and some spatial symmetries, the computational requirements are still quite heavy, with the Hilbert-space size reaching $3.4 \cdot 10^9$ in the undistorted case. Thus, only ED values for $U = 2$ and $U = 5$ are reported, and the missing values were filled in by QMC. The result
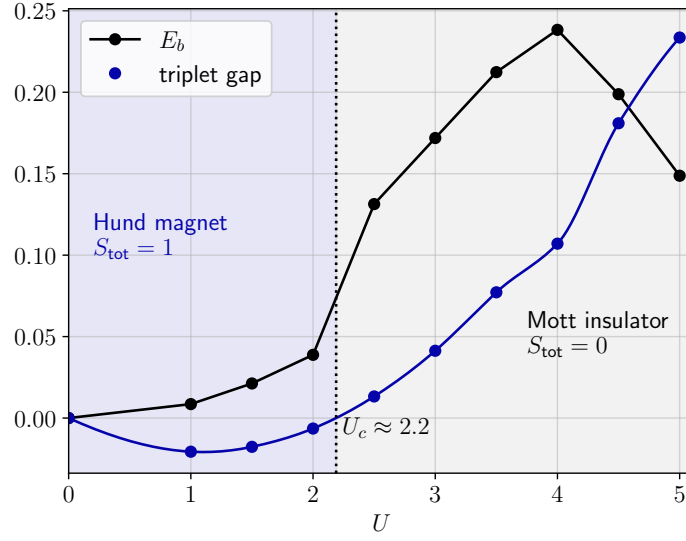
Figure 4: Triplet gap Eq. (4) and pair-binding energy Eq. (1) for C_{20} as a function of U at ~~half filling~~ $N_{\text{tot}} = 20$. $U_c \approx 2.2$ marks the metal-insulator (Mott) transition. Bullets indicate the raw data, lines are a result of Akima spline interpolation (for the triplet gap) or linear interpolation (for E_b).

was a repulsive $E_b > 0$ in the whole U-range, and this was unchanged within the extended Hubbard model [18]. This was surprising in light of the previously demonstrated attractive pair binding for the smaller C_{12} and the cube [5].

The shell structure of C_{20} is metallic, as the HOMO is only partially occupied by two electrons (see Tab. 1). This allows one to study Hund's rule in the half-filled ground state, with the central question being whether the two shell electrons pair to a singlet or triplet. If U is increased, local-moment formation will eventually set in, which results in a singlet ground state that is not due to Hund's rule breaking, but is rather attributed to a Mott transition. For the critical value, $U_c \sim 4.1$ was estimated based on a linear extrapolation of energies between $U = 2$ and $U = 5$ [16].

In Fig. 3, we benchmark our DMRG results for the ground state energy E_0 at $U = 2$ in various sectors of the particle number N_{tot} and the total spin S_{tot} against ED data. Hund's rule is fulfilled at any filling, i.e., the overall ground state features a maximum S_{tot}. We find that the DMRG is precise, with a typical absolute deviation in energy of the order of 10^{-4} (see the data tables in App. C). The DMRG result is accurate enough to clearly resolve the energy gaps between the sectors. For example, for the triplet gap

$$\Delta_1 = E_0\left(N_{\text{tot}}, S_{\text{tot}} = 1\right) - E_0\left(N_{\text{tot}}, S_{\text{tot}} = 0\right) \tag{4}$$

at half filling $N_{\text{tot}} = 20$, ED yields $\Delta_1 = -0.00636$, while the DMRG (extrapolated) value is given by $\Delta_1 = -0.00644$. This needs to be compared to the QMC data where the deviations seem to be at best of order 10^{-3}. Furthermore, QMC suffers from the artifact that the energy depends on the magnetic quantum number for a given S_{tot}, which is strictly not the case within our SU(2)-invariant DMRG approach.

Since the DMRG approach is computationally cheap in comparision to ED, we can readily study arbitrary interactions. Our results are not consistent with the published QMC data in the intermediate-U range. In Figure 4, we plot the triplet gap as a function of U. Using spline interpolation, we place the transition from a metallic Hund magnet to a Mott insulator at $U_c \approx 2.2$, which is significantly smaller than the previously-reported $U_c \sim 4.1$. The smallness of this value entails that one needs to exercise caution when
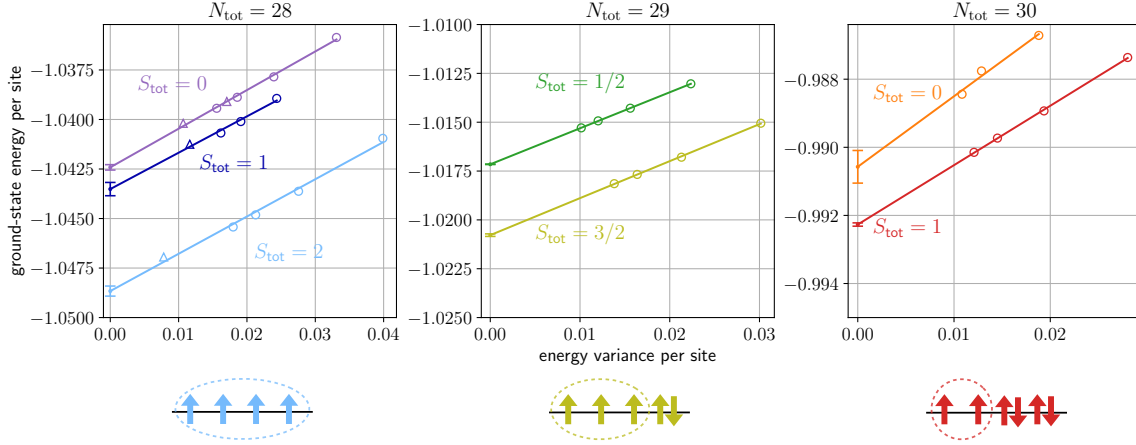
Figure 5: Ground-state energy per site and HOMO filling for C_{28} at $U = 2$. The bond dimensions are $\chi_{SU(2)} \leq 10\,000$ for the SU(2)×U(1)-symmetric calculation (small circles) and $\chi_{SU(2)} = 10\,000, 15\,000$ for the SU(2)×U(1)×$\mathbb{Z}_3$-symmetric calculation (triangles).

extrapolating perturbation theory results to intermediate couplings. We also find that the pair binding energy E_b increases sharply in the region of $U = 3 - 4$ and in fact reaches a local maximum. Nevertheless, we always find $E_b > 0$, i.e., repulsive pair binding in the whole U-region. Note that Eq. (1) at $N_{tot} = 20$ describes pair binding of a system doped with one electron, which is the most relevant case for superconductivity.

4 Molecule C_{28}

C_{28} has tetrahedral symmetry and is metallic like C_{20}. It features a fourfold degenerate HOMO, which is partially occupied by four electrons in the ground state [34–38]. The fourfold degeneracy is a result of an accidental degeneracy of the T_2 and A_1 levels [35]. Due to its protruding tetrahedral bonds, it has been predicted that C_{28} will form a diamond lattice [39–41], but this has not yet been realized chemically.

Figure 5 shows raw DMRG data as well as extrapolated values for the ground-state energy at $U = 2$ in different sectors of N_{tot} and S_{tot}. We clearly see that Hund's rule holds true for all fillings, and the half-filled ground state ($N_{tot} = 28$) is a quintet with $S_{tot} = 2$. Tackling the Hubbard model on C_{28} is considerably more costly than in the case of C_{20}, and the smallest energy variance per site Eq. (3) that can be accessed numerically is larger by one order of magnitude. Consequently, we are unable to precisely evaluate the pair binding energy E_b. A tentative estimate yields $E_b = +0.02 \pm 0.005$ at $U = 2$.

Figure 6 (a) follows the triplet gap Eq. (4) as well as the quintet gap

$$\Delta_2 = E_0(N_{tot}, S_{tot} = 2) - E_0(N_{tot}, S_{tot} = 0) \tag{5}$$

as a function of U at half filling. We see that magnetism is more robust than in the case of C_{20}, and a ground state with $S_{tot} = 2$ persists up to $U_{c,1} \approx 5.4$, after which it becomes a triplet with $S_{tot} = 1$. A transition to a Mott insulator eventually occurs at $U_{c,2} \approx 11.6$. Figure 6 (b) compares the gaps in the Mott insulating phase with those obtained from a strong-coupling Heisenberg model calculation, which allows for an ED solution [42]. We see that the DMRG treatment of the full fermionic problem is in full agreement with the effective Heisenberg model data.
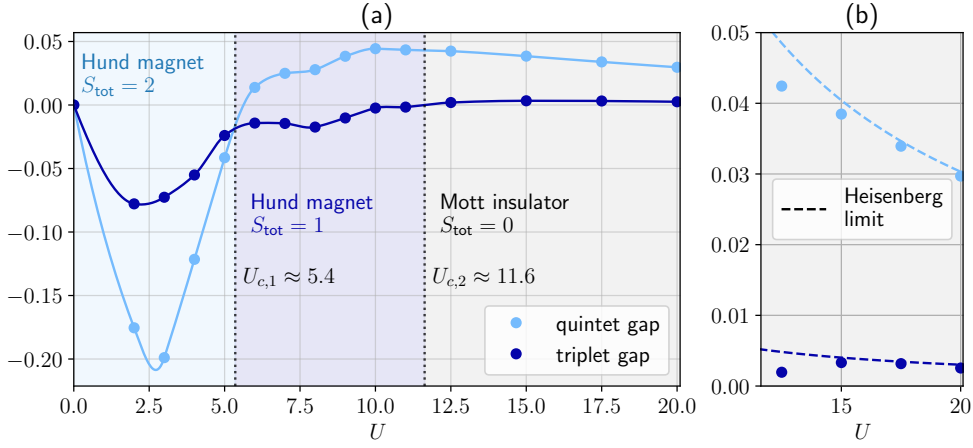
Figure 6: (a) The quintet gap Eq. (5) as well as the triplet gap Eq. (4) for C_{28} as a function of U at half filling $N_{tot} = 28$ (bullets: data, lines: Akima spline interpolation). (b) Zoom-in on the Mott-insulator region. The dashed lines show the Heisenberg limit $(U \gg 1)$ result: $\Delta_i = c_i/U$ with $c_2 = 0.15159$ and $c_1 = 0.01508$ [42].

5 Molecule C_{40} (T_d)

C_{40} has several isomers. The most stable isomer exhibits only a D_{5d} symmetry [43–45] and at most twofold degenerate irreducible representations. For pair binding, we are interested in the more symmetric T_d isomer (see Fig. 1) whose geometry is similar to C_{28}; it is also metallic but has a threefold degenerate HOMO without an accidental degeneracy.

Since tackling C_{40} is numerically costly, we restrict ourselves to $U = 2$, which is a realistic value for carbon and also the point where the pair binding energy peaks for C_{12} [5]. Figure 7 shows raw DMRG data as well as the extrapolated value for the ground-state energy at various N_{tot} and S_{tot}. The smallest site variance that can be accessed in our calculation is a factor of two larger than in the case of C_{28} due to the increased system size and hopping range.

We find that C_{40} exhibits a singlet ground state at half filling with a small gap to the triplet state, indicating Hund's rule breaking. When doped with one electron, however, we find that the maximum-spin sector $S_{tot} = 3/2$ has a slightly lower energy than the one with $S_{tot} = 1/2$. For a doping with two electrons, we are unable to resolve the energies between the sectors $S_{tot} = 0$ and $S_{tot} = 1$. This indicates that there is a tighter competition between the spin sectors for this geometry.

6 Molecule C_{60}

The half-filled ground state of C_{60} is insulating with a completely filled shell, which is analoguous to C_{12} (see Tab. 1). There are thus two relevant energy scales, the band gap $\Delta = 0.757$ and the bandwidth $W = 5.618$. We can discern the following regimes: (i) ultraweak coupling $U < \Delta$, (ii) weak coupling $\Delta < U < W$, (iii) intermediate coupling $U \sim W$, and (iv) strong coupling $U \gg W$. The half-filled ground state is without question a total singlet $S_{tot} = 0$ because of the insulating shell structure, and therefore not of particular interest. In alkali fullerides such as K_3C_{60} [6], there are three doped electrons per C_{60}, which renders the ground state with $N_{tot} = 63$ electrons the most interesting case.

Soon after the advent of the density-matrix renormalization group, the method was applied to C_{60} in momentum space (i.e., using a basis where t_{ij} is diagonal), but only small
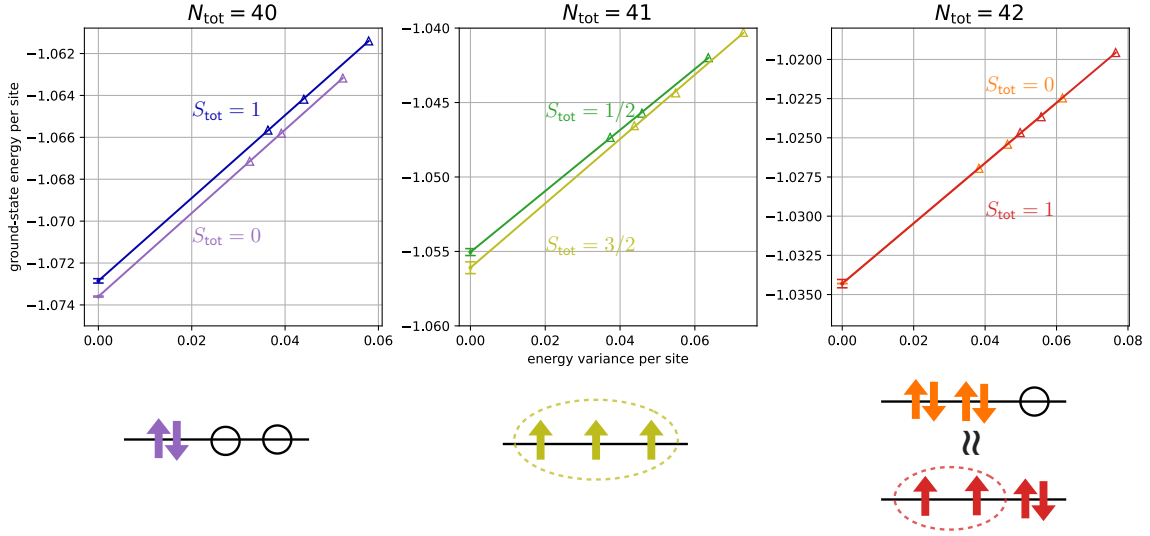
Figure 7: Ground-state energy per site and HOMO filling for C_{40} (T_d) at $U = 2$. Only data for a SU(2)×U(1)×$\mathbb{Z}_3$-symmetric calculation is shown (triangles), and bond dimensions of up to $\chi_{SU(2)} \leq 20\,000$ are employed.

bond dimensions were employed, and the results are only reliable for ultraweak coupling $U \sim 0.001 - 0.01$ [46]. The ground state energy with doping was computed, but the total spin and the pair binding energy were not investigated. In the strong-coupling limit, the undoped Hubbard model simplifies to the Heisenberg model and has been solved with high accuracy using the DMRG [22] as well as via an approach based on neural networks [47]. The undoped strong-coupling limit is useful in understanding the effects of frustration due to the pentagon faces (see App. A), but it is distinct from the doped weak-coupling regime investigated here.

There has been a number of studies in the doped weak-coupling regime. Using QMC, a maximum-spin ground state was found [14]. A minimum-spin ground state was predicted from extrapolating perturbation theory in U [9, 10] and also for the $t - J$ model with a large $J = 0.2 - 1$ [19] using the DMRG with U(1) symmetry. The case $J \to 1$ is assumed to mimic the intermediate-coupling regime with $J = 4t^2/U$ and hence $U/t \sim 4$. However, correction terms such as three-site terms [48] or $O(t^4/U^3)$ contributions [49] have not been considered in this work. Without these corrections, the $t - J$ model should be viewed as similar to, but distinct from the Hubbard model.

C_{60} poses a very tough problem: Since the system size grows by another 50% compared to C_{40} and the hopping range increases further, we find that the best achievable variance per site within the DMRG deteriorates further by one order of magnitude. Furthermore, we observe that the energy variance is larger if the $\mathbb{Z}_5$ symmetry is exploited, so that we restrict ourselves to SU(2)×U(1)-symmetric calculations. The increased hopping range also heightens the risk of getting stuck in a local minimum. We therefore use the following protocol: First, we perform 12 half-sweeps using the two-site algorithm with a bond dimension of $\chi_{SU(2)} = 2500$. We then increase the bond dimension as follows: $2500 \to 5000 \to 6000 \to 7000 \to 8000 \to 9000 \to 10\,000 \to 12\,000 \to 14\,000 \to 16\,000$ and perform 4 half-sweeps at each bond dimension using the one-site algorithm with perturbations. We carry out additional calculations where the bond dimension increases more aggressively, namely $3000 \to 6000 \to 9000 \to 12\,000 \to 15\,000$ as well as $4000 \to 8000 \to 12\,000 \to 16\,000$, and finally $5000 \to 10\,000 \to 15\,000$. This yields five data points with $\chi_{SU(2)} \geq 14\,000$, which use to extrapolate the energy. The result is shown in Fig. 8 for the half-filled ground state
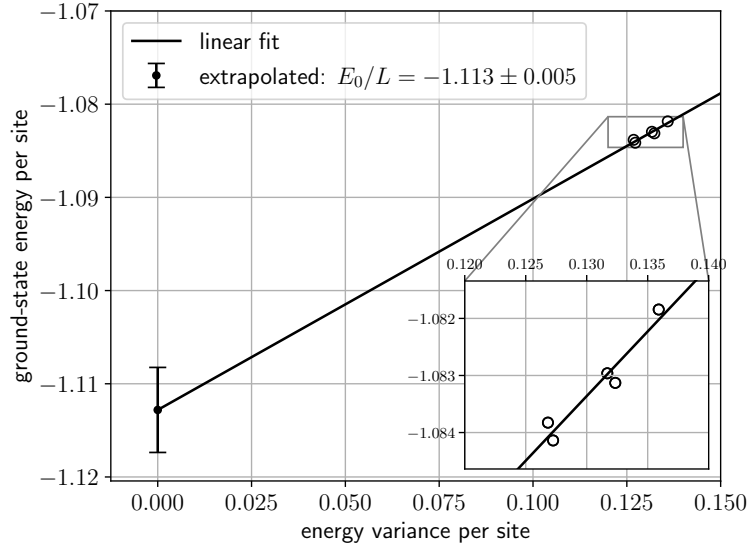
Figure 8: Ground-state energy per site for C_{60} at half filling $N_{tot} = 60$ and a total spin $S_{tot} = 0$ at $U = 2$. Only data for a SU(2)×U(1)-symmetric calculation is shown (small circles). The bond dimensions are in the range $14\,000 \le \chi_{SU(2)} \le 16\,000$.

and in Fig. 9 for finite doping.

Figure 9 illustrates that the energy of a minimum-spin state is below the one of a maximum-spin state for the 2-electron and 3-electron doped case. This is not only true for the extrapolated values, but also at each bond dimension $\chi_{SU(2)}$. For a doping with 4 electrons, we were not able to resolve the energies (similar to the case of C_{40}, see Fig. 7). Overall, our result is ~~consistent~~ in line with both the perturbation theory prediction and the data obtained within the $t - J$ model and ~~supports~~ is consistent with an electronic mechanism for superconductivity in C_{60} lattices. However, the extrapolated energies have overlapping error bounds, so that the confidence of the results for C_{60} is lower than for the smaller molecules. Clearly, more work is needed to improve many-body methods in order to achieve energy variances per site smaller than 10^{-1} for this problem.

7 Discussion

We have investigated Hund's rule breaking in high-symmetry fullerenes C_{20}, C_{28}, C_{40} (T_d), and C_{60} using large-scale DMRG calculations for the Hubbard model.

For C_{20}, we find good agreement with previously-published ED data for $U = 2$ and $U = 5$, but the DMRG approach is numerically cheap and allows us to compute the pair-binding energy as a function of arbitrary U. We find that C_{20} remains repulsive and adheres to Hund's rule in the weak-coupling limit, and we estimate a critical value of $U_c \sim 2.2$ for the metal-insulator transition. The binding energy is repulsive in the whole U-range.

We observe that C_{28} is also adhering to Hund's rule at weak coupling. The half-filled ground state is magnetic with a quintet-triplet transition taking place at $U_{c,1} \sim 5.4$ before a transition to a Mott singlet takes place at $U_{c,2} \sim 11.6$. The typical U-values for carbon $U \sim 2 - 5$ [9, 50, 51] place C_{28} into the quintet Hund magnet phase. A lattice of C_{28} molecules is therefore expected to feature spin-2 sites as the low-energy building blocks. An open question is about the robustness of the spin-2 state towards Jahn-Teller deformations or stabilizer atoms [52].

For C_{40}, the DMRG computation is more expensive and less accurate, and we have only
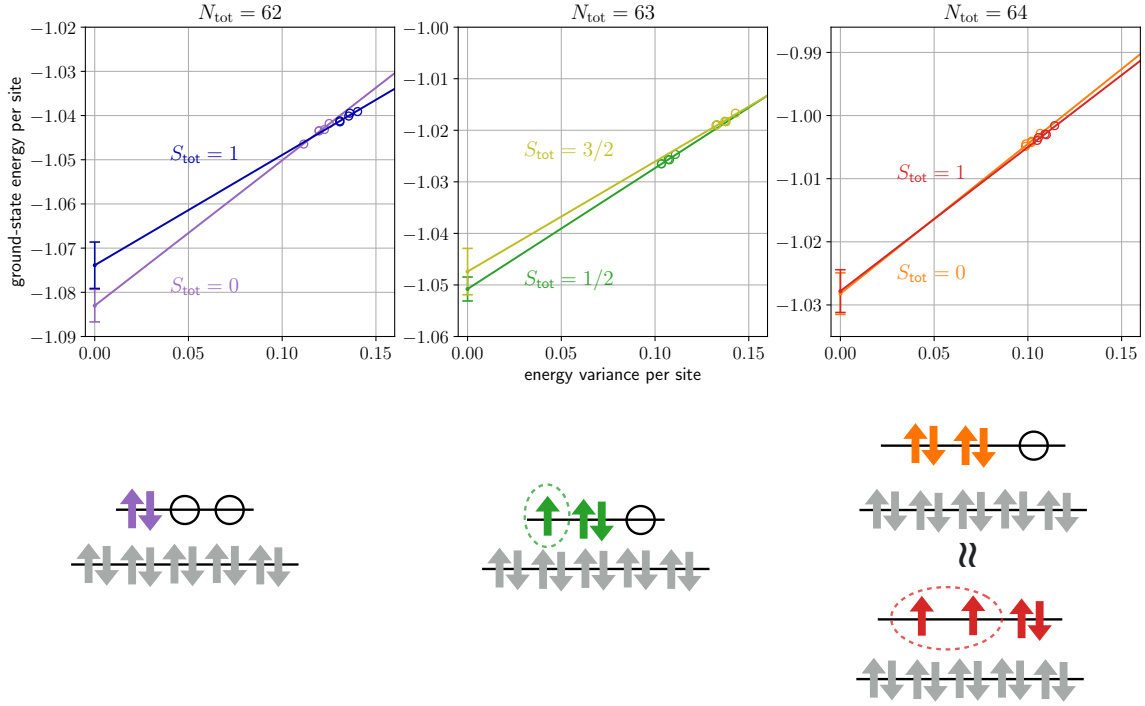
Figure 9: Ground-state energy per site for C_{60} at $U = 2$. Symbols and bond dimensions are as in Fig. 8.

considered $U = 2$. Our result is somewhat ambiguous: we find a singlet for the undoped ground state that breakes Hund's rule but a maximum-spin state when doped with one electron. We were unable to resolve the energies in the different sectors with two doped electrons.

For C_{60}, we document our state-of-the art DMRG results, which we believe to be the best current estimates for the given problem. Our estimate shows Hund's rule breaking at $U = 2$ for the doping with two and three electrons. We were unable to resolve the energies in the sectors with four doped electrons.

Finally, we address the question whether Hund's rule breaking can be connected with a feature in the fullerene geometry. We observe that this breaking becomes more likely with increased fullerene size. The salient geometric feature that also changes with fullerene size is the increase of the number of hexagon faces. Since all fullerenes have exactly 12 pentagon faces, this goes hand-in-hand with a spatial separation of the pentagons (see Fig. 1). Only the pentagons are geometrically frustrated, so that geometric frustration is reduced with the fullerene size, and C_n approaches the unfrustrated hexagonal lattice for large n. The reduced frustration also becomes apparent when studying the spin-only Heisenberg model on the same geometries, which we discuss in App. A. We hence speculate that geometric frustration in fullerenes is detrimental to pair binding and may be the reason why smaller fullerenes are repulsive. In this picture, C_{40} is positioned at the crossover point between repulsive and attractive pair binding, whereas C_{60} is on the attractive side. This is also consistent with the fact that the bipartite and unfrustrated cube shows attractive pair binding [5].

We hope that these results can help guide the selection of molecular building blocks in engineered electron systems, such as metal-organic frameworks [53, 54].

The difficulty of solving the Hubbard model on the C_{60} geometry leads us to propose this system as a benchmark for quantum computing. Previous benchmark systems for quantum simulation were amenable to highly efficient classical tensor-network treat-

ments [55, 56]. But if one flips the perspective and looks at the situation from the tensor-network (MPS) point of view, then C_{60} presents an interesting and hard problem for the classical MPS algorithm, despite being a finite and moderately-sized system. Our paper gives benchmark values using the best possible traditional MPS approach with symmetry exploitation. It would also be interesting if this classical result can be further improved using methods like fermionic orbital optimization [57], adaptive tensor-network geometries [58] or novel techniques based on neural networks [47].

Finally, the computational bottleneck in our approach shifts from ground-state determination to variance evaluation via Eq. (3), which involves calculating H^2 for a long-range Hamiltonian. Our systems can thus also serve as a testing ground for algorithms that aim to provide cheaper variance estimates [59].

Acknowledgements

Discussions with Matthias Peschke are gratefully acknowledged.

A Strong-coupling limit

For reasons of completeness, we summarize the properties of the fullerenes in the strong-coupling limit $U \gg 1$. Except for C_{40}, this is a compilation of results known from existing literature.

The low-energy behaviour in the strong-coupling limit is governed by the Heisenberg model

$$H = \sum_{ij} J_{ij} \mathbf{S}_i \cdot \mathbf{S}_j, \qquad (6)$$

where J_{ij} is the matrix of exchange interactions that has the same structure as t_{ij}, and $\mathbf{S}_i = (S_i^x, S_i^y, S_i^z)$ is the vector of spin operators. We set $J_{ij} = 1$ between nearest neighbours.

In the Heisenberg model, the effect of strong frustration manifests itself in low-lying singlet states below the first triplet, and sometimes also in a degenerate ground state. The former effect entails that low-lying excitations are unconventional and different from magnons (spinflips), while the latter implies symmetry breaking in the form of a valence-bond-solid-like state.

Table 2 shows a summary of the strong-coupling results. For C_{40}, which was not studied before, we calculate the low-lying states of Eq. (6) using a SU(2)-invariant DMRG algorithm with a bond dimension of $\chi_{SU(2)} = 2000$, which translates into an energy variance per site of $\sim 10^{-5}$, which is sufficient to estimate the gaps.

C_{12} and C_{60} are characterized by spinflip excitations, i.e., the smallest gap is the triplet gap; the gaps are rather large and the ground states are unique. C_{12} and C_{60} can be viewed as weakly frustrated: Their lattices are non-bipartite, but the triangle and pentagon plaquettes are not able to induce the abovementioned prototypical features of frustrated spin systems.

The lowest excitations for C_{20} and C_{40} are singlets. For C_{28}, they are a triplet, but the ground state for both C_{28} and C_{40} is twofold degenerate. In fact, the ordinary tetrahedron has a twofold degenerate ground state which features singlet coverings, and this property seems to be transferred to tetrahedral C_{20} and C_{40}. We categorize C_{20}, C_{28}, and C_{40} as strongly frustrated.

molecule	g.s. deg.	singlet gap	triplet gap	reference	frustration
C_{12}	1	0.896	**0.688**	[60]	weak
C_{20}	1	**0.316**	0.514	[61]	strong
C_{28}	2	0.0702	**0.015**	[42]	strong
C_{40} (T_d)	2	**0.04(2)**	0.13(3)	this work	strong
C_{60}	1	0.691	**0.356**	[22, 47]	weak

Table 2: Properties of the molecules at strong coupling $U \gg 1$, Eq. (6): ground-state degeneracy, singlet gap $\Delta_0 = E_1\left(S_{\text{tot}} = 0\right) - E_0\left(S_{\text{tot}} = 0\right)$, triplet gap $\Delta_1 = E_0\left(S_{\text{tot}} = 1\right) - E_0\left(S_{\text{tot}} = 0\right)$. The smaller gap is shown in bold.
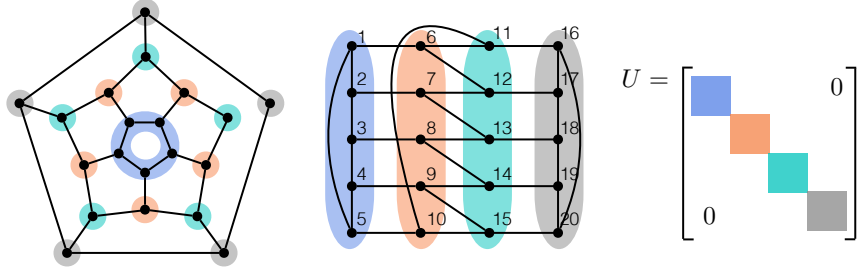
Figure 10: Left: Schlegel diagram of the C_{20} hopping matrix with the points connected by $\mathbb{Z}_5$ rotations shaded in the same color. Middle: The same graph, but deformed to a ladder-like structure with the points connected by rotations placed on the rungs. The depicted enumeration of the sites leads to a maximal hopping range of 6 (see Tab. 2). Right: The unitary transformation that rotates the molecule is block-diagonal.

B $\mathbb{Z}_N$ symmetry

In this section, we explain how to exploit the $\mathbb{Z}_N$ molecular symmetry in the DMRG code.

1. We start from a Schlegel diagram of the molecule and identify the sites that belong to the same cycle of length N, i.e., those that transform into each other under the $\mathbb{Z}_N$ symmetry operation of the graph (see Fig. 10, left).

2. We enumerate the sites such that the sites within each cycle are enumerated in consecutive order (see Fig. 10, center).

3. Each cycle is an $N \times N$ matrix (often circulant), which we interpret as the one-particle kinetic Hamiltonian $\underline{H}_{\text{cycle}}$. We construct the full $L \times L$ hopping matrix $\underline{t}$, where the cycles are diagonal blocks that are further connected by inter-cycle hopping terms.

4. An operator that permutes two fermions on the sites i and j is given by $P_{ij} = 1 - n_i - n_j + c_i^\dagger c_j + c_j^\dagger c_i$ [62]. On the single-particle level, this can be constructed explicitly as $\underline{P}_{ij} = I_N - n_{ij} + h_{ij}$, where I_N is the $N \times N$ identity matrix, n_{ij} has entries equal to $+1$ at (i,i), (j,j); h_{ij} has entries equal to $+1$ at (i,j), (j,i); and both are 0 otherwise. A product of the corresponding $\underline{P}_{ij}$ over a cycle defines the unitary operation $\underline{U}_{\text{cycle}}$ that permutes the fermions according to this symmetry.

5. Since $\underline{U}_{\text{cycle}}$ is a symmetry, the matrices $\underline{H}_{\text{cycle}}$ and $\underline{U}_{\text{cycle}} = \exp\left(\frac{2\pi i}{N}\underline{A}\right)$ (with hermitian $\underline{A}$) commute and therefore have common eigenvectors, which can be found by simultaneous diagonalization. We furthermore permute the result so that the eigenvectors correspond to increasing eigenvalues $J = 0, 1, \ldots N-1$ (pseudo-angular

momenta) of $\underline{A}$. This permutation is an additional unitary transformation that can be grouped together with $\underline{U}_{\mathrm{cycle}}$.

6. The unitary transformation $\underline{U}$ for the full $L \times L$ system is assembled as a block matrix from the individual blocks of the cycles $\underline{U}_{\mathrm{cycle}}$ (see Fig. 10, right).

7. $\underline{U}$ can be carried over to the many-body regime by letting it act on the creation and annihilation operators, $c^\dagger_{\mathbf{k}\sigma} = \sum_i U_{i\mathbf{k}} c^\dagger_{i\sigma}$ and $c^\dagger_{i\sigma} = \sum_{\mathbf{k}} U^*_{i\mathbf{k}} c^\dagger_{\mathbf{k}\sigma}$, where we use the bold letters to indicate the transformed orbitals. The single-particle hopping matrix $\underline{t}$ is transformed according to

$$\underline{t} \;\mapsto\; \underline{U}^\dagger \, \underline{t} \, \underline{U}.$$

This defines a list of new hopping terms $c^\dagger_{\mathbf{k}\sigma} c_{\mathbf{l}\sigma}$ ($\mathbf{k} \neq \mathbf{l}$) and on-site terms $n_{\mathbf{k}} = c^\dagger_{\mathbf{k}\sigma} c_{\mathbf{k}\sigma}$ with the corresponding coefficients for the transformed Hamiltonian. Each site can now be labeled by the quantum number J. Each term is a product of operators and can be trivially encoded by an MPO of bond dimension 1.

8. Next, we apply the unitary transformation $\underline{U}$ to interaction term of Eq. (2) and similarly get a list of 4-fermion terms

$$U \sum_i \sum_{\mathbf{klmn}} U^*_{i\mathbf{k}} U_{i\mathbf{l}} U^*_{i\mathbf{m}} U_{i\mathbf{n}} c^\dagger_{\mathbf{k}\uparrow} c_{\mathbf{l}\uparrow} c^\dagger_{\mathbf{m}\downarrow} c_{\mathbf{n}\downarrow} = V_{\mathbf{klmn}} c^\dagger_{\mathbf{k}\uparrow} c_{\mathbf{l}\uparrow} c^\dagger_{\mathbf{m}\downarrow} c_{\mathbf{n}\downarrow}, \qquad (7)$$

whereby some of the coefficients $V_{\mathbf{klmn}}$ vanish by angular momentum conservation. We would like the individual terms to be encoded by MPOs of bond dimension 1 again, but this is somewhat more difficult when exploiting spin-SU(2), since intermediate spin exchange is involved. We thus have to go through the additional step of grouping the terms by the SU(2)-invariant processes (assuming $\mathbf{k}$, $\mathbf{l}$, $\mathbf{m}$, $\mathbf{n}$ are all distinct):

- double occupancy: $n_{\mathbf{k}\uparrow} n_{\mathbf{k}\downarrow}$
- correlated hopping: $c^\dagger_{\mathbf{l}\sigma} n_{\mathbf{k}} c_{\mathbf{k}\sigma}$
- doublon hopping: $c^\dagger_{\mathbf{k}\uparrow} c^\dagger_{\mathbf{k}\downarrow} c_{\mathbf{l}\downarrow} c_{\mathbf{l}\uparrow}$
- spin exchange: $\mathbf{S}_{\mathbf{k}} \cdot \mathbf{S}_{\mathbf{l}} = \frac{1}{2} \sum_{\sigma,\sigma'} c^\dagger_{\mathbf{k}\sigma} c_{\mathbf{l}\sigma} c^\dagger_{\mathbf{l}\sigma'} c_{\mathbf{k}\sigma'} - \frac{1}{4} n_{\mathbf{k}} n_{\mathbf{l}}$
- 3-site correlated hopping: $n_{\mathbf{k}} c^\dagger_{\mathbf{l}\sigma} c_{\mathbf{m}\sigma}$
- 3-site spin exchange: $c^\dagger_{\mathbf{k}\uparrow} c_{\mathbf{k}\downarrow} c^\dagger_{\mathbf{l}\downarrow} c_{\mathbf{m}\uparrow}$ and the corresponding density terms like $n_{\mathbf{k}\sigma} c^\dagger_{\mathbf{l}\sigma} c_{\mathbf{m}\sigma}$
- doublon creation/decay: $c^\dagger_{\mathbf{k}\uparrow} c^\dagger_{\mathbf{k}\downarrow} c_{\mathbf{l}\uparrow} c_{\mathbf{m}\downarrow}$
- generic 4-site terms: $c^\dagger_{\mathbf{i}\uparrow} c^\dagger_{\mathbf{j}\downarrow} c_{\mathbf{k}\uparrow} c_{\mathbf{l}\downarrow}$

For each process, a sum over a dangling spin index yields an operator that can be represented by reduced matrix elements that are used in the spin-SU(2) DMRG code (see Ref. [63] for more details), and we finally arrive at a list of operators, where we know how to encode every single one as an MPO.

9. Finally, we need to sum up all the resulting contributions to the Hamiltonian and represent the result as a large MPO. To reduce the bond dimension of the resulting sum, we employ the lossless compression algorithm from Ref. [29]. We also compute and compress H^2, which is needed to evaluate the energy variance.

C   Data

bond dim.	symmetry	variance per site	E	E/L
4000	SU(2)×U(1)	2.565129e-03	-20.5872319308	-1.0293615965
6000	SU(2)×U(1)	8.677940e-04	-20.5905735288	-1.0295286764
8000	SU(2)×U(1)	4.137779e-04	-20.5913712010	-1.0295685600
10000	SU(2)×U(1)	1.841385e-04	-20.5917551483	-1.0295877574
15000	SU(2)×U(1)×$\mathbb{Z}_5$	1.949971e-05	-20.5919949945	-1.0295997497
	extrap.		-20.5921159527	-1.0296057976
	extrap. error			± 2.40e-06
	ED		-20.5920234655	-1.0296011733

Table 3: Data for C_{20}, $N_{\mathrm{tot}} = 20$, $S = 0$

bond dim.	symmetry	variance per site	E	E/L
4000	SU(2)×U(1)	4.424098e-03	-20.5892218077	-1.0294610904
6000	SU(2)×U(1)	1.692830e-03	-20.5952048339	-1.0297602417
8000	SU(2)×U(1)	8.590140e-04	-20.5968201969	-1.0298410098
10000	SU(2)×U(1)	5.062640e-04	-20.5974541920	-1.0298727096
15000	SU(2)×U(1)×$\mathbb{Z}_5$	7.491663e-05	-20.5982741549	-1.0299137077
	extrap.		-20.5985585526	-1.0299279276
	extrap. error			± 4.55e-06
	ED		-20.5983834340	-1.0299191717

Table 4: Data for C_{20}, $N_{\mathrm{tot}} = 20$, $S = 1$

bond dim.	symmetry	variance	E	E/L
4000	SU(2)×U(1)	3.201929e-03	-19.6152315449	-0.9807615772
6000	SU(2)×U(1)	1.137871e-03	-19.6195522755	-0.9809776138
8000	SU(2)×U(1)	5.003695e-04	-19.6207223803	-0.9810361190
10000	SU(2)×U(1)	2.753801e-04	-19.6211024980	-0.9810551249
	extrap.		-19.6217371459	-0.9810868573
	extrap. error			± 3.77e-06

Table 5: Data for C_{20}, $N_{\mathrm{tot}} = 21$, $S = 1/2$

bond dim.	symmetry	variance per site	E	E/L
4000	SU(2)×U(1)	3.972304e-03	-19.6250885367	-0.9812544268
6000	SU(2)×U(1)	1.319480e-03	-19.6308550666	-0.9815427533
8000	SU(2)×U(1)	6.407885e-04	-19.6321219916	-0.9816060996
10000	SU(2)×U(1)	5.515291e-04	-19.6322537303	-0.9816126865
	extrap.		-19.6334998929	-0.9816749946
	extrap. error			± 4.52e-06
	ED		-19.6331786587	-0.9816589329

Table 6: Data for C_{20}, $N_{\text{tot}} = 21$, $S = 3/2$

bond dim.	symmetry	variance per site	E	E/L
4000	SU(2)×U(1)	3.990221e-03	-18.4926020619	-0.9246301031
6000	SU(2)×U(1)	1.659147e-03	-18.4982504217	-0.9249125211
8000	SU(2)×U(1)	7.934607e-04	-18.4999343862	-0.9249967193
10000	SU(2)×U(1)	4.152969e-04	-18.5006117934	-0.9250305897
	extrap.		-18.5017311225	-0.9250865561
	extrap. error			± 9.61e-06

Table 7: Data for C_{20}, $N_{\text{tot}} = 22$, $S = 0$

bond dim.	symmetry	variance per site	E	E/L
4000	SU(2)×U(1)	9.982944e-03	-18.5316139161	-0.9265806958
6000	SU(2)×U(1)	4.060265e-03	-18.5492792649	-0.9274639632
8000	SU(2)×U(1)	2.016879e-03	-18.5536790937	-0.9276839547
10000	SU(2)×U(1)	1.150801e-03	-18.5553590813	-0.9277679541
	extrap.		-18.5592232767	-0.9279611638
	extrap. error			± 3.95e-05

Table 8: Data for C_{20}, $N_{\text{tot}} = 22$, $S = 1$

bond dim.	symmetry	variance per site	E	E/L
4000	SU(2)×U(1)	7.393416e-03	-18.6123479933	-0.9306173997
6000	SU(2)×U(1)	2.299429e-03	-18.6247204396	-0.9312360220
8000	SU(2)×U(1)	1.093284e-03	-18.6270716327	-0.9313535816
10000	SU(2)×U(1)	5.856133e-04	-18.6279847528	-0.9313992376
	extrap.		-18.6296398753	-0.9314819938
	extrap. error			± 1.36e-05
	ED		-18.6289129089	-0.9314456454

Table 9: Data for C_{20}, $N_{\text{tot}} = 22$, $S = 2$

bond dim.	symmetry	variance per site	E	E/L
4000	SU(2)×U(1)	3.309751e-02	-29.0040627605	-1.0358593843
6000	SU(2)×U(1)	2.392813e-02	-29.0597492572	-1.0378481878
8000	SU(2)×U(1)	1.858130e-02	-29.0886396069	-1.0388799860
10000	SU(2)×U(1)	1.557305e-02	-29.1041762882	-1.0394348674
10000	SU(2)×U(1)×$\mathbb{Z}_3$	1.705322e-02	-29.0945838181	-1.0394583818
15000	SU(2)×U(1)×$\mathbb{Z}_3$	1.067015e-02	-29.1254247543	-1.0416949836
	extrap.		-29.1876642696	-1.0424165811
	extrap. error			± 1.36e-04

Table 10: Data for C$_{28}$, $N_{\text{tot}} = 28$, $S = 0$

bond dim.	symmetry	variance per site	E	E/L
6000	SU(2)×U(1)	2.435410e-02	-29.0902358560	-1.0389369949
8000	SU(2)×U(1)	1.910066e-02	-29.1229364748	-1.0401048741
10000	SU(2)×U(1)	1.618168e-02	-29.1390964008	-1.0406820143
15000	SU(2)×U(1)×$\mathbb{Z}_3$	1.163410e-02	-29.1549763442	-1.0435705219
	extrap.		-29.2183821028	-1.0435136465
	extrap. error			± 3.35e-04

Table 11: Data for C$_{28}$, $N_{\text{tot}} = 28$, $S = 1$

bond dim.	symmetry	variance per site	E	E/L
4000	SU(2)×U(1)	3.988430e-02	-29.1466539737	-1.0409519276
6000	SU(2)×U(1)	2.755306e-02	-29.2214757364	-1.0436241334
8000	SU(2)×U(1)	2.126947e-02	-29.2548318766	-1.0448154242
10000	SU(2)×U(1)	1.798120e-02	-29.2719640371	-1.0454272870
15000	SU(2)×U(1)×$\mathbb{Z}_3$	7.816843e-03	-29.3143776753	-1.0472852883
	extrap.		-29.3625532877	-1.0486626174
	extrap. error			± 2.54e-04

Table 12: Data for C$_{28}$, $N_{\text{tot}} = 28$, $S = 2$

bond dim.	symmetry	variance per site	E	E/L
4000	SU(2)×U(1)	2.234914e-02	-28.3649459528	-1.0130337840
6000	SU(2)×U(1)	1.560330e-02	-28.3999200061	-1.0142828574
8000	SU(2)×U(1)	1.201980e-02	-28.4180663036	-1.0149309394
10000	SU(2)×U(1)	1.013856e-02	-28.4281043806	-1.0152894422
	extrap.		-28.4803208909	-1.0171543175
	extrap. error			± 1.19e-05

Table 13: Data for C$_{28}$, $N_{\text{tot}} = 29$, $S = 1/2$

bond dim.	symmetry	variance per site	E	E/L
4000	SU(2)×U(1)	3.014672e-02	-28.4214379836	-1.0150513566
6000	SU(2)×U(1)	2.130527e-02	-28.4701504827	-1.0167910887
8000	SU(2)×U(1)	1.637474e-02	-28.4948253567	-1.0176723342
10000	SU(2)×U(1)	1.381529e-02	-28.5080689822	-1.0181453208
	extrap.		-28.5818529420	-1.0207804622
	extrap. error			± 6.48e-05

Table 14: Data for C$_{28}$, $N_{\text{tot}} = 29$, $S = 3/2$

bond dim.	symmetry	variance per site	E	E/L
4000	SU(2)×U(1)	1.880715e-02	-27.6280266150	-0.9867152362
6000	SU(2)×U(1)	1.285464e-02	-27.6572331402	-0.9877583264
8000	SU(2)×U(1)	1.083324e-02	-27.6763647794	-0.9884415993
	extrap.		-27.7360290388	-0.9905724657
	extrap. error			± 4.79e-04

Table 15: Data for C_{28}, $N_{tot} = 30$, $S = 0$

bond dim.	symmetry	variance per site	E	E/L
4000	SU(2)×U(1)	2.804127e-02	-27.6461636143	-0.9873629862
6000	SU(2)×U(1)	1.934873e-02	-27.6900722315	-0.9889311511
8000	SU(2)×U(1)	1.451294e-02	-27.7124380716	-0.9897299311
10000	SU(2)×U(1)	1.207910e-02	-27.7241404241	-0.9901478723
	extrap.		-27.7834955238	-0.9922676973
	extrap. error			± 4.86e-05

Table 16: Data for C_{28}, $N_{tot} = 30$, $S = 1$

bond dim.	symmetry	variance per site	E	E/L
10000	SU(2)×U(1)×$\mathbb{Z}_3$	5.236308e-02	-42.5267938821	-1.0631698471
15000	SU(2)×U(1)×$\mathbb{Z}_3$	3.919015e-02	-42.6321080424	-1.0658027011
20000	SU(2)×U(1)×$\mathbb{Z}_3$	3.240451e-02	-42.6856841714	-1.0671421043
	extrap.		-42.9439945371	-1.0735998634
	extrap. error			± 2.62e-05

Table 17: Data for C_{40} (T_d), $U = 2$, $N_{tot} = 40$, $S = 0$

bond dim.	symmetry	variance per site	E	E/L
10000	SU(2)×U(1)×$\mathbb{Z}_3$	5.790364e-02	-42.4558585233	-1.0613964631
15000	SU(2)×U(1)×$\mathbb{Z}_3$	4.401479e-02	-42.5671663123	-1.0641791578
20000	SU(2)×U(1)×$\mathbb{Z}_3$	3.632150e-02	-42.6261792769	-1.0656544820
	extrap.		-42.9140624943	-1.0728515624
	extrap. error			± 1.04e-04

Table 18: Data for C_{40} (T_d), $U = 2$, $N_{tot} = 40$, $S = 1$

bond dim.	symmetry	variance per site	E	E/L
10000	SU(2)×U(1)×$\mathbb{Z}_3$	6.358959e-02	-41.6794911022	-1.0160827086
15000	SU(2)×U(1)×$\mathbb{Z}_3$	4.585133e-02	-41.8286384995	-1.0202097195
20000	SU(2)×U(1)×$\mathbb{Z}_3$	3.733541e-02	-41.8937502589	-1.0217999600
	extrap.		-42.2017435255	-1.0550435881
	extrap. error			± 2.32e-04

Table 19: Data for C_{40} (T_d), $U = 2$, $N_{tot} = 41$, $S = 1/2$

bond dim.	symmetry	variance per site	E	E/L
10000	SU(2)×U(1)×$\mathbb{Z}_3$	7.296366e-02	-41.6114621999	-1.0149141039
15000	SU(2)×U(1)×$\mathbb{Z}_3$	5.487482e-02	-41.7740646212	-1.0198574251
20000	SU(2)×U(1)×$\mathbb{Z}_3$	4.382172e-02	-41.8622101077	-1.0222492477
	extrap.		-42.2437454703	-1.0560936368
	extrap. error			± 3.95e-04

Table 20: Data for C$_{40}$ (T$_d$), $U = 2$, $N_{\text{tot}} = 41$, $S = 3/2$

bond dim.	symmetry	variance per site	E	E/L
10000	SU(2)×U(1)×$\mathbb{Z}_3$	6.166042e-02	-40.8982491011	-0.9737687881
15000	SU(2)×U(1)×$\mathbb{Z}_3$	4.627591e-02	-41.0163720665	-0.9765802873
20000	SU(2)×U(1)×$\mathbb{Z}_3$	3.826717e-02	-41.0779820901	-0.9770948120
	extrap.		-41.3719340340	-1.0342983508
	extrap. error			± 4.63e-06

Table 21: Data for C$_{40}$ (T$_d$), $U = 2$, $N_{\text{tot}} = 42$, $S = 0$

bond dim.	symmetry	variance per site	E	E/L
10000	SU(2)×U(1)×$\mathbb{Z}_3$	7.654455e-02	-40.7824406642	-0.9719633482
15000	SU(2)×U(1)×$\mathbb{Z}_3$	5.568845e-02	-40.9462019109	-0.9749095693
17500	SU(2)×U(1)×$\mathbb{Z}_3$	4.981659e-02	-40.9866775903	-0.9758732760
	extrap.		-41.3721808204	-1.0343045205
	extrap. error			± 2.65e-04

Table 22: Data for C$_{40}$ (T$_d$), $U = 2$, $N_{\text{tot}} = 42$, $S = 1$

bond dim.	symmetry	variance per site	E	E/L
14000	SU(2)×U(1)	0.135904022658	-64.9106586457	-1.0818443108
16000	SU(2)×U(1)	0.126821199128	-65.0295658490	-1.0838260975
15000	SU(2)×U(1)	0.131687812195	-64.9776993639	-1.0829616561
16000	SU(2)×U(1)	0.127244207774	-65.0483095680	-1.0841384928
15000	SU(2)×U(1)	0.132342386810	-64.9877664803	-1.0831294413
	extrap.		-66.7684664015	-1.1128077734
	extrap. error			± 4.56e-03

Table 23: Data for C$_{60}$, $N_{\text{tot}} = 60$, $S = 0$

bond dim.	symmetry	variance per site	E	E/L
14000	SU(2)×U(1)	0.111483782545	-62.7869028882	-1.0464483815
16000	SU(2)×U(1)	0.119667635466	-62.6074120632	-1.0434568677
15000	SU(2)×U(1)	0.122541374362	-62.5895070252	-1.0431584504
16000	SU(2)×U(1)	0.119667635466	-62.6074120632	-1.0434568677
15000	SU(2)×U(1)	0.125065586486	-62.5078200406	-1.0417970007
	extrap.		-64.9810150219	-1.0830169170
	extrap. error			± 3.68e-03

Table 24: Data for C$_{60}$, $N_{\text{tot}} = 62$, $S = 0$

bond dim.	symmetry	variance per site	E	E/L
14000	SU(2)×U(1)	0.140217832409	-62.3458427788	-1.0390973796
16000	SU(2)×U(1)	0.130731479726	-62.4721647664	-1.0412027461
12000	SU(2)×U(1)	0.156120435903	-62.0839421370	-1.0347323689
15000	SU(2)×U(1)	0.136095093591	-62.3679731374	-1.0394662190
16000	SU(2)×U(1)	0.130812101335	-62.4860542411	-1.0414342374
15000	SU(2)×U(1)	0.135490162120	-62.4069163987	-1.0401152733
	extrap.		-64.4325029349	-1.0738750489
	extrap. error			$\pm$ 5.25e-03

Table 25: Data for C_{60}, $N_{tot} = 62$, $S = 1$

bond dim.	symmetry	variance per site	E	E/L
14000	SU(2)×U(1)	0.110868648671	-61.4808743475	-1.0246812391
16000	SU(2)×U(1)	0.103413283990	-61.5898491564	-1.0264974859
12000	SU(2)×U(1)	0.122382340505	-61.3438622710	-1.0223977045
15000	SU(2)×U(1)	0.107002037933	-61.5394676338	-1.0256577939
16000	SU(2)×U(1)	0.103413283990	-61.5898491564	-1.0264974859
15000	SU(2)×U(1)	0.107709551776	-61.5438874189	-1.0257314570
	extrap.		-63.0470844675	-1.0507847411
	extrap. error			$\pm$ 2.32e-03

Table 26: Data for C_{60}, $N_{tot} = 63$, $S = 1/2$

bond dim.	symmetry	variance per site	E	E/L
14000	SU(2)×U(1)	0.142897022042	-61.0008014205	-1.0166800237
16000	SU(2)×U(1)	0.132975317242	-61.1337803719	-1.0188963395
15000	SU(2)×U(1)	0.137260244327	-61.0940647523	-1.0182344125
16000	SU(2)×U(1)	0.132512468442	-61.1414905453	-1.0190248424
15000	SU(2)×U(1)	0.137905519692	-61.1007579958	-1.0183459666
	extrap.		-62.8444741267	-1.0474079021
	extrap. error			$\pm$ 4.50e-03

Table 27: Data for C_{60}, $N_{tot} = 63$, $S = 3/2$

bond dim.	symmetry	variance per site	E	E/L
14000	SU(2)×U(1)	0.106587928114	-60.1702174621	-1.0028369577
16000	SU(2)×U(1)	0.0989582789575	-60.2697980478	-1.0044966341
15000	SU(2)×U(1)	0.101934726830	-60.2443643559	-1.0040727393
16000	SU(2)×U(1)	0.0987337990014	-60.2928024167	-1.0048800403
15000	SU(2)×U(1)	0.101869205715	-60.2563401115	-1.0042723352
	extrap.		-61.6926752737	-1.0282112546
	extrap. error			$\pm$ 3.29e-03

Table 28: Data for C_{60}, $N_{tot} = 64$, $S = 0$

bond dim.	symmetry	variance per site	E	E/L
14000	SU(2)×U(1)	0.114286443750	-60.0958895711	-1.0015981595
16000	SU(2)×U(1)	0.105624198492	-60.2093091792	-1.0034884863
15000	SU(2)×U(1)	0.109141837355	-60.1757886515	-1.0029298109
16000	SU(2)×U(1)	0.104981742230	-60.2358369592	-1.0039306160
15000	SU(2)×U(1)	0.109864076307	-60.1825244363	-1.0030420739
	extrap.		-61.6684749901	-1.0278079165
	extrap. error			± 3.39e-03

Table 29: Data for C_{60}, $N_{tot} = 64$, $S = 1$

References

[1] F. Hund, *Zur Deutung verwickelter Spektren, insbesondere der Elemente Scandium bis Nickel*, Zeitschrift für Physik **33**(1), 345 (1925), doi:10.1007/BF01328319.

[2] J. Katriel and R. Pauncz, *Theoretical interpretation of Hund's Rule*, vol. 10 of *Advances in Quantum Chemistry*, pp. 143–185. Academic Press, doi:https://doi.org/10.1016/S0065-3276(08)60580-8 (1977).

[3] R. A. Broglia and V. Zelevinsky, *Fifty years of nuclear BCS: pairing in finite systems*, World Scientific (2013).

[4] V. Zelevinsky and A. Volya, *Physics of Atomic Nuclei*, John Wiley & Sons (2017).

[5] S. R. White, S. Chakravarty, M. P. Gelfand and S. A. Kivelson, *Pair binding in small Hubbard-model molecules*, Phys. Rev. B **45**, 5062 (1992), doi:10.1103/PhysRevB.45.5062.

[6] T. Palstra, O. Zhou, Y. Iwasa, P. Sulewski, R. Fleming and B. Zegarski, *Superconductivity at 40K in cesium doped C_{60}*, Solid State Communications **93**(4), 327 (1995), doi:https://doi.org/10.1016/0038-1098(94)00787-X.

[7] Y. Takabayashi and K. Prassides, *Unconventional high-T_c superconductivity in fullerides*, Philosophical Transactions of the Royal Society A: Mathematical, Physical and Engineering Sciences **374**(2076), 20150320 (2016), doi:10.1098/rsta.2015.0320.

[8] S. Chakravarty and S. A. Kivelson, *Electronic mechanism of superconductivity in the cuprates, c_{60}, and polyacenes*, Phys. Rev. B **64**, 064511 (2001), doi:10.1103/PhysRevB.64.064511.

[9] S. Chakravarty and S. Kivelson, *Superconductivity of doped fullerenes*, Europhysics Letters **16**(8), 751 (1991), doi:10.1209/0295-5075/16/8/008.

[10] S. Chakravarty, M. P. Gelfand and S. Kivelson, *Electronic correlation effects and superconductivity in doped fullerenes*, Science **254**(5034), 970 (1991), doi:10.1126/science.254.5034.970.

[11] L. Bergomi, J. P. Blaizot, T. Jolicoeur and E. Dagotto, *Generalized spin-density-wave state of the Hubbard model for c_{12} and c_{60} clusters*, Phys. Rev. B **47**, 5539 (1993), doi:10.1103/PhysRevB.47.5539.

[12] R. T. Scalettar, A. Moreo, E. Dagotto, L. Bergomi, T. Jolicoeur and H. Monien, *Ground-state properties of the Hubbard model on a c_{60} cluster*, Phys. Rev. B **47**, 12316 (1993), doi:10.1103/PhysRevB.47.12316.

[13] M. Lüders, A. Bordoni, N. Manini, A. D. Corso, M. Fabrizio and E. Tosatti, *Coulomb couplings in positively charged fullerene*, Philosophical Magazine B **82**(15), 1611 (2002), doi:10.1080/13642810208220729, https://doi.org/10.1080/13642810208220729.

[14] F. Lin, J. **S**makov, E. S. Sørensen, C. Kallin and A. J. Berlinsky, *Quantum monte carlo calculation of the electronic binding energy in a c_{60} molecule*, Phys. Rev. B **71**, 165436 (2005), doi:10.1103/PhysRevB.71.165436.

[15] N. Manini and E. Tosatti, *Theoretical aspects of highly correlated fullerides: metal-insulator transition*, arXiv preprint cond-mat/0602134 (2006).

[16] F. Lin, E. S. Sørensen, C. Kallin and A. J. Berlinsky, *Strong correlation effects in the fullerene* c_{20} *studied using a one-band Hubbard model*, Phys. Rev. B **76**, 033414 (2007), doi:10.1103/PhysRevB.76.033414.

[17] F. Lin, E. S. Sørensen, C. Kallin and A. J. Berlinsky, *Single-particle excitation spectra of* c_{60} *molecules and monolayers*, Phys. Rev. B **75**, 075112 (2007), doi:10.1103/PhysRevB.75.075112.

[18] F. Lin, E. S. Sørensen, C. Kallin and A. J. Berlinsky, *Extended Hubbard model on a* c_{20} *molecule*, Journal of Physics: Condensed Matter **19**(45), 456206 (2007), doi:10.1088/0953-8984/19/45/456206.

[19] H.-C. Jiang and S. Kivelson, *Electronic pair binding and hund's rule violations in doped* c_{60}, Phys. Rev. B **93**, 165406 (2016), doi:10.1103/PhysRevB.93.165406.

[20] U. Schollwöck, *The density-matrix renormalization group in the age of matrix product states*, Annals of Physics **326**(1), 96 (2011), doi:https://doi.org/10.1016/j.aop.2010.09.012, January 2011 Special Issue.

[21] M. Exler and J. Schnack, *Evaluation of the low-lying energy spectrum of magnetic keplerate molecules using the density-matrix renormalization group technique*, Phys. Rev. B **67**, 094440 (2003), doi:10.1103/PhysRevB.67.094440.

[22] R. Rausch, C. Plorin and M. Peschke, *The antiferromagnetic* $S = 1/2$ *Heisenberg model on the* C_{60} *fullerene geometry*, SciPost Phys. **10**, 087 (2021), doi:10.21468/SciPostPhys.10.4.087.

[23] R. Rausch, M. Peschke, C. Plorin and C. Karrasch, *Magnetic properties of a capped kagome molecule with 60 quantum spins*, SciPost Phys. **12**, 143 (2022), doi:10.21468/SciPostPhys.12.5.143.

[24] R. Rausch and C. Karrasch, *The low-spin ground state of the giant Mn wheels* (2024), `2401.07552`.

[25] G. K.-L. Chan and S. Sharma, *The density matrix renormalization group in quantum chemistry*, Annual Review of Physical Chemistry **62**(1), 465 (2011), doi:10.1146/annurev-physchem-032210-103338, PMID: 21219144, `https://doi.org/10.1146/annurev-physchem-032210-103338`.

[26] R. Rausch, M. Peschke, C. Plorin, J. Schnack and C. Karrasch, *Quantum spin spiral ground state of the ferrimagnetic sawtooth chain*, SciPost Phys. **14**, 052 (2023), doi:10.21468/SciPostPhys.14.3.052.

[27] C. Hubig, I. P. McCulloch, U. Schollwöck and F. A. Wolf, *Strictly single-site DMRG algorithm with subspace expansion*, Phys. Rev. B **91**, 155115 (2015), doi:10.1103/PhysRevB.91.155115.

[28] G. K.-L. Chan and M. Head-Gordon, *Highly correlated calculations with a polynomial cost algorithm: A study of the density matrix renormalization group*, The Journal of Chemical Physics **116**(11), 4462 (2002), doi:10.1063/1.1449459, `https://pubs.aip.org/aip/jcp/article-pdf/116/11/4462/19222618/4462_1_online.pdf`.

[29] C. Hubig, I. P. McCulloch and U. Schollwöck, *Generic construction of efficient matrix product operators*, Phys. Rev. B **95**, 035129 (2017), doi:10.1103/PhysRevB.95.035129.

[30] I. P. McCulloch and M. Gulácsi, *The non-abelian density matrix renormalization group algorithm*, Europhysics Letters **57**(6), 852 (2002), doi:10.1209/epl/i2002-00393-0.

[31] J. Motruk, M. P. Zaletel, R. S. K. Mong and F. Pollmann, *Density matrix renormalization group on a cylinder in mixed real and momentum space*, Phys. Rev. B **93**, 155139 (2016), doi:10.1103/PhysRevB.93.155139.

[32] G. Ehlers, S. R. White and R. M. Noack, *Hybrid-space density matrix renormalization group study of the doped two-dimensional Hubbard model*, Phys. Rev. B **95**, 125125 (2017), doi:10.1103/PhysRevB.95.125125.

[33] A. Szasz, J. Motruk, M. P. Zaletel and J. E. Moore, *Chiral spin liquid phase of the triangular lattice Hubbard model: A density matrix renormalization group study*, Phys. Rev. X **10**, 021042 (2020), doi:10.1103/PhysRevX.10.021042.

[34] M. Feyereisen, M. Gutowski, J. Simons and J. Almlöf, *Relative stabilities of fullerene, cumulene, and polyacetylene structures for C_n: $n = 18\breve{}60$*, The Journal of Chemical Physics **96**(4), 2926 (1992), doi:10.1063/1.461989.

[35] P. W. Fowler, S. J. Austin and J. P. B. Sandall, *The tetravalence of C_{28}*, J. Chem. Soc., Perkin Trans. 2 pp. 795–797 (1993), doi:10.1039/P29930000795.

[36] G. Klimko, M. Mestechkin, G. Whyman and S. Khmelevsky, *C_{28} and c_{48} fullerenes special properties*, Journal of Molecular Structure **480-481**, 329 (1999), doi:https://doi.org/10.1016/S0022-2860(98)00815-1.

[37] P. W. Dunk, N. K. Kaiser, M. Mulet-Gas, A. Rodríguez-Fortea, J. M. Poblet, H. Shinohara, C. L. Hendrickson, A. G. Marshall and H. W. Kroto, *The smallest stable fullerene, M@C_{28} (M = Ti, Zr, U): Stabilization and growth from carbon vapor*, Journal of the American Chemical Society **134**(22), 9380 (2012), doi:10.1021/ja302398h.

[38] A. V. Silant'ev, *Energy spectrum and optical properties of fullerene C_{28} within the Hubbard model*, Physics of Metals and Metallography **121**(6), 501 (2020), doi:10.1134/S0031918X20060149.

[39] D. M. Bylander and L. Kleinman, *Calculated properties of polybenzene and hyperdiamond*, Phys. Rev. B **47**, 10967 (1993), doi:10.1103/PhysRevB.47.10967.

[40] E. Kaxiras, L. M. Zeger, A. Antonelli and Y.-m. Juan, *Electronic properties of a cluster-based solid form of carbon: C_{28} hyperdiamond*, Phys. Rev. B **49**, 8446 (1994), doi:10.1103/PhysRevB.49.8446.

[41] E. Kaxiras, *Atomic and electronic structure of solids*, Cambridge University Press, ISBN 0521523397 (2003).

[42] N. P. Konstantinidis, *$s = \frac{1}{2}$ antiferromagnetic Heisenberg model on fullerene-type symmetry clusters*, Phys. Rev. B **80**, 134427 (2009), doi:10.1103/PhysRevB.80.134427.

[43] R. Salcedo and L. Sansores, *Electronic structure of C_{40} possible structures*, Journal of Molecular Structure: THEOCHEM **422**(1), 245 (1998), doi:https://doi.org/10.1016/S0166-1280(97)00111-5.

[44] M. Cui, H. Zhang, M. Ge, J. Feng, W. Tian and C. Sun, *An ab initio study of C_{40}, C_{40}^+, $C_{40}h_4$, Nb^+@C_{40}, $Nb^+ C_{39}$ and Nb^+@$C_{40}h_4$ clusters*, Chemical Physics Letters **309**(5), 344 (1999), doi:https://doi.org/10.1016/S0009-2614(99)00716-2.

[45] X. Yang, G. Wang, Z. Shang, Y. Pan, Z. Cai and X. Zhao, *A systematic investigation on the molecular behaviors of boron- or nitrogen-doped C_{40} cluster*, Phys. Chem. Chem. Phys. **4**, 2546 (2002), doi:10.1039/B111443C.

[46] S. Qin, J. Lou, Z. Su and L. Yu, *Strongly correlated complex systems*, In I. Peschel, M. Kaulke, X. Wang and K. Hallberg, eds., *Density-Matrix Renormalization*, pp. 271–278. Springer Berlin Heidelberg, Berlin, Heidelberg, ISBN 978-3-540-48750-0 (1999).

[47] A. Szabó, S. Capponi and F. Alet, *Noncoplanar and chiral spin states on the way towards Néel ordering in fullerene Heisenberg models*, Phys. Rev. B **109**, 054410 (2024), doi:10.1103/PhysRevB.109.054410.

[48] B. Ammon, M. Troyer and H. Tsunetsugu, *Effect of the three-site hopping term on the t-J model*, Phys. Rev. B **52**, 629 (1995), doi:10.1103/PhysRevB.52.629.

[49] L. N. Bulaevskiĭ, *Quasihomopolar electron levels in crystals and molecules*, Soviet Journal of Experimental and Theoretical Physics **24**, 154 (1967).

[50] T. O. Wehling, E. Şaşıoğlu, C. Friedrich, A. I. Lichtenstein, M. I. Katsnelson and S. Blügel, *Strength of effective Coulomb interactions in graphene and graphite*, Phys. Rev. Lett. **106**, 236805 (2011), doi:10.1103/PhysRevLett.106.236805.

[51] W. Barford, *Electronic and Optical Properties of Conjugated Polymers*, Oxford University Press, ISBN 9780199677467, doi:10.1093/acprof:oso/9780199677467.001.0001 (2013).

[52] Y. Makurin, A. Sofronov, A. Gusev and A. Ivanovsky, *Electronic structure and chemical stabilization of c_{28} fullerene*, Chemical Physics **270**(2), 293 (2001), doi:https://doi.org/10.1016/S0301-0104(01)00342-1.

[53] V. Guillerm, D. Kim, J. F. Eubank, R. Luebke, X. Liu, K. Adil, M. S. Lah and M. Eddaoudi, *A supermolecular building approach for the design and construction of metal–organic frameworks*, Chem. Soc. Rev. **43**, 6141 (2014), doi:10.1039/C4CS00135D.

[54] A. E. Thorarinsdottir and T. D. Harris, *Metal–organic framework magnets*, Chemical Reviews **120**(16), 8716 (2020), doi:10.1021/acs.chemrev.9b00666, PMID: 32045215, https://doi.org/10.1021/acs.chemrev.9b00666.

[55] S. Patra, S. S. Jahromi, S. Singh and R. Orús, *Efficient tensor network simulation of IBM's largest quantum processors*, Phys. Rev. Res. **6**, 013326 (2024), doi:10.1103/PhysRevResearch.6.013326.

[56] J. Tindall, M. Fishman, E. M. Stoudenmire and D. Sels, *Efficient tensor network simulation of IBM's eagle kicked ising experiment*, PRX Quantum **5**, 010308 (2024), doi:10.1103/PRXQuantum.5.010308.

[57] C. Krumnow, L. Veis, O. Legeza and J. Eisert, *Fermionic orbital optimization in tensor network states*, Phys. Rev. Lett. **117**, 210402 (2016), doi:10.1103/PhysRevLett.117.210402.

[58] S. Patra, S. Singh and R. Orús, *Projected entangled pair states with flexible geometry*, Phys. Rev. Res. **7**, L012002 (2025), doi:10.1103/PhysRevResearch.7.L012002.

[59] J. M. Silvester, G. Carleo and S. R. White, *Unusual energy spectra of matrix product states* (2025), 2408.13616.

[60] D. Coffey and S. A. Trugman, *Correlations for the $s = 1/2$ antiferromagnet on a truncated tetrahedron*, Phys. Rev. B **46**, 12717 (1992), doi:10.1103/PhysRevB.46.12717.

[61] N. P. Konstantinidis, *Antiferromagnetic Heisenberg model on clusters with icosahedral symmetry*, Phys. Rev. B **72**, 064453 (2005), doi:10.1103/PhysRevB.72.064453.

[62] F. H. Essler, H. Frahm, F. Göhmann, A. Klümper and V. E. Korepin, *The one-dimensional Hubbard model*, Cambridge University Press (2005).

[63] S. Keller and M. Reiher, *Spin-adapted matrix product states and operators*, The Journal of Chemical Physics **144**(13), 134101 (2016), doi:10.1063/1.4944921.